INTERNATIONAL JOURNAL of RENEWABLE ENERGY RESEARCH
S. Imad ud din et al., Vol.13, No.3, September, 2023

Performance Analysis of a Novel Photovoltaic Thermal PVT Double Pass Solar Air Heater with Cylindrical PCM Capsules using CFD

Sahibzada Imad ud din*, Adnan Ibrahim*‡, Ahmad Fazlizan*, Amir Aziat Ishak*, Faisal Nawab**, Ag Sufiyan Abd Hamid***†

* Solar Energy Research Institute, Universiti Kebangsaan Malaysia, 43600, Bangi, Selangor, Malaysia

** Department of Renewable Energy, Khushal Khan Khattak University, Karak, KPK, Pakistan

*** Faculty of Science and Natural Resources, Universiti Malaysia Sabah, 88400 Kota Kinabalu, Sabah, Malaysia

(immiedwardian@gmail.com, iadnan@ukm.edu.my, a.fazlizan@ukm.edu.my, amirishak93@yahoo.com, fnawab17@gmail.com, pian@ums.edu.my)

‡Adnan Ibrahim, Solar Energy Research Institute, Universiti Kebangsaan Malaysia,
43600, Bangi, Selangor, Malaysia, Tel: + 60 389118581, iadnan@ukm.edu.my

†Ag Sufiyan Abd Hamid, Faculty of Science and Natural Resources, Universiti Malaysia Sabah,
88400 Kota Kinabalu, Sabah, Malaysia, Tel; +6088 320000, pian@ums.edu.my

Received: 19.04.2023 Accepted:11.06.2023

Abstract- Photovoltaic Thermal Double Pass Solar Air Heater (PVT-DPSAH) with Phase Change Material (PCM) capsules in the bottom channel is a promising design for enhancing the system performance. The PVT-DPSAH comprises a glass cover, absorber plate photovoltaic (PV), PCM capsules, and back plate. The current study uses COMSOL Multiphysics software to perform a Computational Fluid Dynamics (CFD) analysis of a novel PVT-DPSAH with vertical cylindrical PCM capsules in the second channel. To solve the differential equations in the 3D computational domain, the Finite Element Method (FEM) is employed. This study uses the high Reynolds (Re) number and κ-ε turbulent flow model with enhanced wall functions. The impact of varying solar irradiance levels (500-800 W/m^2) on the performance of PVT-DPSAH, with mass flow rate ($\dot{m}$) ranging from 0.011 kg/s to 0.065 kg/s, is investigated. The optimum mass flow rate was found to be 0.037 kg/s at solar irradiances ranging from 500 W/m^2 to 800 W/m^2, with average thermal efficiencies, electrical efficiencies, and fluid output temperatures of 60.7% to 63.4%, 11.25% to 11.02% and 42.96 ℃ to 49.54 ℃, respectively. PVT collector's maximum combined efficiency was 84.12% at solar irradiance of 800 W/m^2 with the mass flow rate, $\dot{m}$ of 0.065 kg/s. This study identified RT-47 paraffin-wax-PCM as the best option for the PVT-DPSAH based on the PCM's thermal distribution and melting temperature.

Keywords Photovoltaic Thermal (PVT), Double Pass Solar Air Heater (DPSAH), PVT-DPSAH, PCM, Paraffin-Wax, Heat transfer, CFD simulation

1. Introduction

Solar energy conversion has captivated the interest of researchers more than other renewable technologies due to its infinite and cost-free availability on the entire surface of the earth [1], [2]. The effective use and gathering of solar energy are necessary for reducing reliance on fossil fuels. In the current realm of solar-powered systems, the thermal industry is a prevalent field of exploration and innovation, extending from household cooking to thermal energy facilities [3], [4]. The most basic, cost-effective, and popular method for capturing and transforming solar energy into heat is through a solar air heater collector. The Solar Air Heater (SAH) mainly consists of three parts: an absorber plate, a cover made of glazing material, and wall insulation. The absorption surface and the glazed cover create a duct for airflow. The SAH has a wide range of uses, including heating spaces, drying, industrial processing, and seasoning timber [5]. Single-pass (SP) type or Single Pass Solar Air Heater (SPSAH) and Double-Pass (DP) type or DPSAH are the two most common types of basic solar air heater. The SPSAH has an air duct between the cover and the absorber sheet. In contrast, the DPSAH type has two passes for air flow circulation. The first pass is an enclosed air gap that separates the transparent cover and collector plate. The second pass is the bottom layer, separated by the air gap between the collector and the bottom plate. The primary reason for the prevalent use of DPSAH's is their improved thermal efficiency [6]. The efficiency of these systems depends on a variety of different elements, such as the design of the channels, flow rates, and the characteristics of the material that makes up the absorbing collector. Researchers have tried various methods, including adding protrusions, fins, ribs, winglets, artificial roughness, porous beds, and turbulence promoters to the absorber plate and the second layer, to increase the thermal efficiency and heat transfer rate of the DPSAH [7]–[14].

PV systems have greatly improved, with modern panels collecting over 75% of the sun's energy and converting up to 18% into usable electricity. The efficiency of a panel depends on temperature and solar irradiation, with optimal efficiency between 25 ºC and 30 ºC and 900-1000 W/m^2 of solar irradiation. Beyond this range, the efficiency of the cell can decrease by up to 0.65% per degree Celsius increase. Controlling the temperature rise is essential to maintain a panel's peak operational condition. PVT system combines PV cells and thermal collectors to extract heat for useful purposes. Recent PVT technology allows cells to operate at optimal efficiency while providing thermal energy. The overall efficiency of the hybrid design is determined by the combined efficiency of both (thermal and electrical) systems. Extracted heat can be utilized effectively in a PVT system, making it more efficient and cost-effective, as the heat is utilized alongside the generated electricity [15]. PCM is widely recognized as a valuable component of solar thermal systems because it can store and release significant amounts of energy as latent heat [16]–[18]. Klemm et al. presented a thermal storage approach incorporated with PCM to boost the efficiency of PV panels by combining PCM with the metallic fiber structures on the back of the solar module. A numerical study was performed using COMSOL Multiphysics. This method has been reported to result in a 20 ºC decrease in the daily peak temperature [19]. Kumar et al. investigated the effectiveness of a PVT-DPSAH, including vertical fins in the bottom channel, and its effect on PV surface temperature [9]. Research on PVT systems has led to the development of more effective systems. Studies have shown that absorbers made of aluminium fins are the most efficient regarding the SAH's combined efficiency. Heat and electricity may be generated when solar PV panels are coupled with a storage solar water heater [20]. However, managing the surface temperature is crucial as the panel's efficiency decreases noticeably as the temperature rises. Nevertheless, the efficiency of this system depends on a variety of different elements, such as the design of the channels, flow rates, and the characteristics of the material that makes up the absorber. Therefore, thorough investigations of the system's performance behaviour are required for optimal design and operations. CFD modelling is a significant tool that can help provide insight into the performance of the system and assist in optimising it.

CFD is a scientific technique for studying complex fluid dynamics phenomena such as heat transfer, fluid movement, and solidification/melting behaviour. CFD analysis solves governing equations through numerical techniques, which allows for the modification of designs, optimization, troubleshooting, and validation of experimental discoveries. CFD allows for modelling many different physical and boundary conditions, some of which would be impossible or impractical to simulate using traditional experimental methods [21], [22]. The current study uses CFD to numerically investigate the performance and PCM temperature distribution in the second channel of a novel PVT-DPSAH. This study aims to accomplish the following objectives:

- To examine the effects of cylindrical shape capsules on the fluid output temperature, velocity flow, and temperature distribution in the PCM.
- To analyze how variables, e.g., mass flow rate and solar irradiance, affect the PVT-DPSAH efficiency.
- To analyze PV surface temperature, thermal, electrical, and combined efficiency (thermal and electrical).
- To identify the appropriate PCM type to be used based on the temperature distribution in the second channel.

2. Computational Analysis

2.1. Description of The CFD Model

The proposed PVT-DPSAH with cylindrical encapsulated PCM capsules is presented in Fig 1. The geometry comprises transparent glazing glass, a PV collector plate, cylindrical PCM capsules, and the back plate. The absorber plate measures 2.40 m in length and 0.54 m in width. The absorber plate and glass thicknesses are 0.003 m and 0.004 m, respectively. The upper and second layer depths are 0.035 m and 0.075 m, respectively.

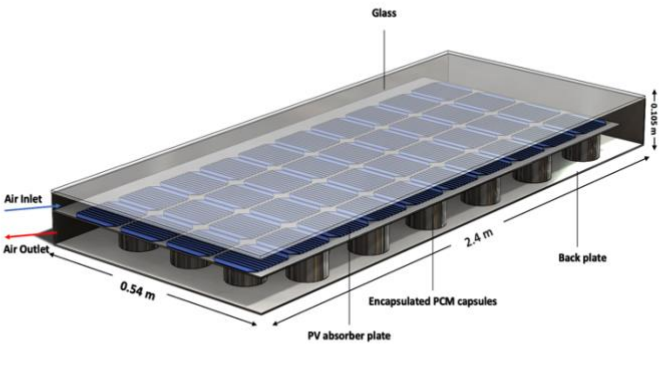

Fig 1. Proposed PVT Double Pass Solar Air Heater

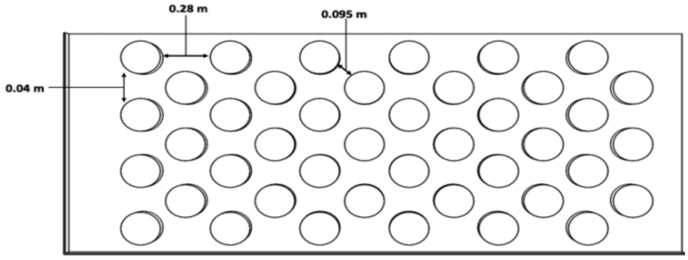

Fig 2. Staggered Cylindrical PCM capsules configuration in the second channel

The cylindrical encapsulated PCM has a diameter of 0.05 m, and there are 42 cylinders aligned in a staggered configuration (Fig 2).

2.2. Computational Domain and Boundary Conditions

For this study, a numerical analysis was conducted using a steady-state condition. The equations controlling the air's temperature and velocity depended on mass, momentum, and energy conservation principles. A convergence criterion of 10^{-5}, 10^{-5}, and 10^{-7} was chosen for continuity, velocity, and energy, respectively. The analysis used a conjugate heat transfer module to compute the interaction between heat transfer in solid and fluid domains. A turbulent flow k-e model was used, as it is suitable for high RE numbers and weakly compressible flows [23]. The primary characteristics and physical attributes of the investigated PVT DPSAH are tabulated in Tables 1 and 2.

COMSOL CFD includes temperature-dependent features for analyzing air properties, glass, and absorber plate material (aluminium). Flow velocities at solid surfaces are assumed to be constant and non-slip. Under the assumption that the glass is perfectly transparent and does not absorb or emit radiation, the collector's upper surface receives the same amount of irradiation. A boundary condition is established where the glass is open to ultraviolet radiation. The average velocity of the fluid entering the system is calculated using the RE numbers, and the inlet condition of the boundary is specified as "Velocity Inlet" while the system's outlet was specified as "Pressure Outlet" at 1.013 x 10^{13} Pa atmospheric pressure. The absorber plate is subjected to 500, 600, 700, and 800 W/m^2 of constant and uniform heat flux. Initial and ambient system temperatures were both set to 30 ºC. The remaining system walls are considered adiabatic, meaning they do not exchange heat with their surroundings.

As shown in Fig 3, the top glass cover and the back plate were subjected to forced convective boundary conditions. The equations used to estimate the top surface glass convective heat flux are shown in Eq. 1-2:

$$q_0 = h(T_{\text{ext}} - T) \tag{1}$$

$$h = \begin{cases} \frac{k}{L} 0.54 \mathrm{Ra}_L^{1/4} & \text{if } T > T_{\text{ext}} \text{ and } 10^4 \le \mathrm{Ra}L \le 10^7 \\ \frac{k}{L} 0.15 \mathrm{Ra}_L^{1/3} & \text{if } T > T_{\text{ext}} \text{ and } 10^7 \le \mathrm{Ra}L \le 10^{11} \\ \frac{k}{L} 0.27 \mathrm{Ra}_L^{1/4} & \text{if } T \le T_{\text{ext}} \text{ and } 10^5 \le \mathrm{Ra}L \le 10^{10} \end{cases} \tag{2}$$

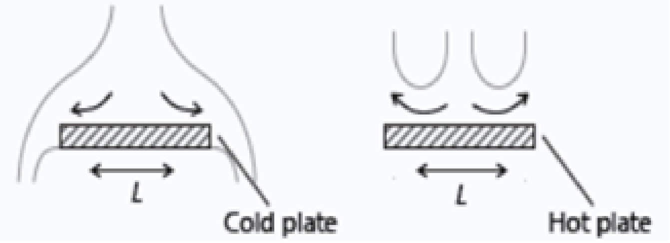

Fig 3. Top surface force convection [24]

Where L is the characteristic length and k is the thermal conductivity of the material. Figure 4 shows the forced convection boundary condition on the back plate. The convective flux can be calculated by Eq. 3:

$$h = \begin{cases} \frac{k}{L} 0.54 \mathrm{Ra}_L^{1/4} & \text{if } T \le T_{\text{ext}} \text{ and } 10^4 \le \mathrm{Ra}L \le 10^7 \\ \frac{k}{L} 0.15 \mathrm{Ra}_L^{1/3} & \text{if } T \le T_{\text{ext}} \text{ and } 10^7 \le \mathrm{Ra}L \le 10^{11} \\ \frac{k}{l} 0.27 \mathrm{Ra}_L^{1/4} & \text{if } T > T_{\text{ext}} \text{ and } 10^5 \le \mathrm{Ra}L \le 10^{10} \end{cases} \tag{3}$$

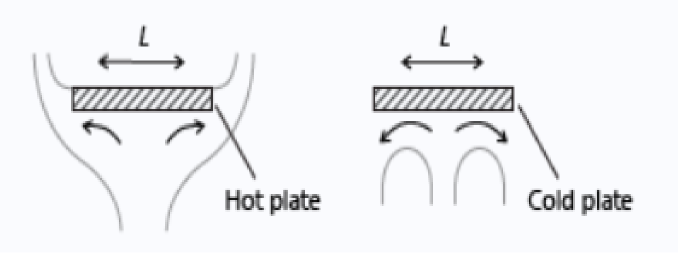

Fig 4. Bottom surface forced convection [24]

For phase change material:

- The transition from solid to liquid occurs at a temperature of 47 ºC.
- Latent heat from phase 1 to phase 2 is 210[kJ/kg].

For the stationary study, the phase change was calculated using Eqs. 4 - 8 [24]:

$$\rho = \theta_1 \rho_1 + \theta_2 \rho_2 \tag{4}$$

$$c_p = \frac{1}{\rho}\left(\theta_1 \rho_1 C_{p,1} + \theta_2 \rho_2 C_{p,2}\right) + L_{1\to 2} \frac{\partial \alpha_m}{\partial T} \tag{5}$$

$$\alpha_m = \frac{1}{2} \frac{\theta_2 \rho_2 - \theta_1 \rho_1}{\theta_1 \rho_1 + \theta_2 \rho_2} \tag{6}$$

$$k = \theta_1 k_1 + \theta_2 k_2 \tag{7}$$

$$\theta_1 + \theta_2 = 1 \tag{8}$$

Table 1. Parameters of PVT-DPSAH

Parameter	Value
Absorber plate length	2.4m
Absorber plate width	0.54m
Absorber plater area	1.29m
PV Panel thickness	0.002m
Glazing cover thickness	0.003m
Height of cylindrical fins	0.075m
Diameter of cylindrical fins	0.05m
Number of cylindrical fins	42
Inlet reference Temperature	30 ^oC
Absorber thermal conductivity	211 W/m^2.K
Insulation Thickness	0.05m
Solar Irradiance (W/m^2)	500, 600, 700, 800
Mass flow rate ($\dot{m}$)	0.01 - 0.06 kg/s
Temperature coefficient (β_{ref})	0.0045 k^{-1}
Reference electrical efficiency (η_{ref})	0.16
Packing Factor (P)	0.80
Reference Temperature (T_{ref})	30 ^oC

Table 2. Physical properties of materials

Material	Thermal Conductivity (W/m^2 K)	Density (kg/m^3)	Heat Capacity (J/kg k)	Emissivity	Absorbtivity
Air	0.0262	1.17	1005.7	-	-
Glass	1.4	2210	730	0.84	0.05
Aluminium	238	2700	900	0.90	0.95
Foam	0.026	70	1045	-	-
PCM Solid	0.211	880	2200	-	-
PCM Liquid	0.214	770	2100	-	-

2.3. Selection and Validation of Turbulent Solver

Different turbulence methods have been developed to predict turbulence in fluid movement, including Direct Numerical Simulation (DNS), Large Eddy Simulation (LES), and Reynolds Averaged Navier-Stokes (RANS). While DNS provides highly accurate results, it is computationally expensive, whereas LES requires fewer computational resources. Among these methods, RANS is the most commonly used technique in industrial applications for analyzing turbulent flows, as it strikes a balance between computational efficiency and accuracy. The κ-ε, k-w, and Shear Stress Transport (SST) models are commonly used RANS models that produce accurate results with computational efficiency. The κ-ε model is widely used in investigations of SAH's (SPSAH and DPSAH) [25]–[28].

The turbulent behaviour is analyzed with the help of the κ-ε model in this research. The model is inaccurate near walls, so wall functions were used to account for this [29]. This two-equation model is established in CFD and considers realizability constraints. It uses κ and ε variables for turbulent kinetic energy and dissipation rate. The κ-ε model has been employed in various DPSAH studies using CFD, and it is computationally efficient while maintaining acceptable accuracy [23], [30]. Equations 9 to 11 are used to calculate turbulent flow [31]:

$$\mu_{\mathrm{T}} = \rho c_{\mu} \frac{k^2}{\epsilon} \tag{9}$$

$$\rho(\mathbf{u} \cdot \nabla)k = \nabla \cdot \left[\left(\mu + \frac{\mu_T}{\sigma_{\mathrm{k}}}\right) \nabla k\right] + P_{\mathrm{k}} - \rho\epsilon \tag{10}$$

$$\rho(\mathbf{u} \cdot \nabla)\epsilon = \nabla \cdot \left[\left(\mu + \frac{\mu_T}{\sigma_{\epsilon}}\right) \nabla \epsilon\right] + C_{\epsilon 1} \frac{\epsilon}{k} P_{\mathrm{k}} - C_{\epsilon 2} \rho \frac{\epsilon^2}{k} \tag{11}$$

2.4. Mesh Generation

In most cases, computational domains can be divided into meshes using structured elements, which are in a quad shape, unstructured, triangular, or a combination of both, known as hybrid elements. The decision to use a particular mesh type depends on the physical properties of the flow, such as whether it's laminar or turbulent, and the problem's geometry, such as whether it's curved or straight. To improve convergence time and guarantee a high-quality mesh, a test for mesh independence was conducted for this study. The meshes generated were physics-controlled meshes. Figure 5 shows the generated mesh for various qualities. It can be seen that mesh near the walls is enhanced progressively due to the κ-ε model. Table 3 shows the thermal efficiency results conducted at 600 W/m^2 and includes increasing mesh elements to the point when the solution attained constant results.

Table 3. Mesh Independence Study at 600 W/m^2

Element Size	No of Elements	$\dot{m}$ (kg/s)	Thermal efficiency (%)
Extremely Coarse	200269	0.06	71.30
Coarser	478709	0.06	70.12
Coarse	770704	0.06	69.78
Normal	2086411	0.06	69.25
Fine	6470359	0.06	69.20
Finer	26736702	0.06	69.17

2.5. Selection and Validation of The CFD Model

The heat transfer and turbulent models were validated against Moustafa et al. [23]. They used COMSOL Multiphysics V5.3a to design three models of DPSAH and compared them with the experimental results. CFD model dimensions and boundary conditions were generated based on the numerical investigations of DPSAH's of Ismail A.F et al. [32] and J. Assadeg et al. [33]. Table 4 compares operating conditions, design parameters $\dot{m}$=0.01-0.06 kg/s, and solar irradiance ranges from 500 to 800 W/m^2 with the previous work. Only thermal efficiency has been compared for validation purposes.

Furthermore, cylindrical PCM capsules are added in the second channel. The temperature distribution in the PCM capsules has been analyzed. The phase-change process was modelled using an enthalpy-porosity (EP) approach [34]. A fixed grid is assumed to simulate a single volume of the same material containing solid and liquid PCM. The melting point was kept constant at 47 ℃ throughout the investigation. The transition from solid to liquid occurred at a constant rate as a function of temperature. Table 5 lists the constant values for the thermophysical characteristics of paraffin wax (RT47) in both its solid and liquid states.

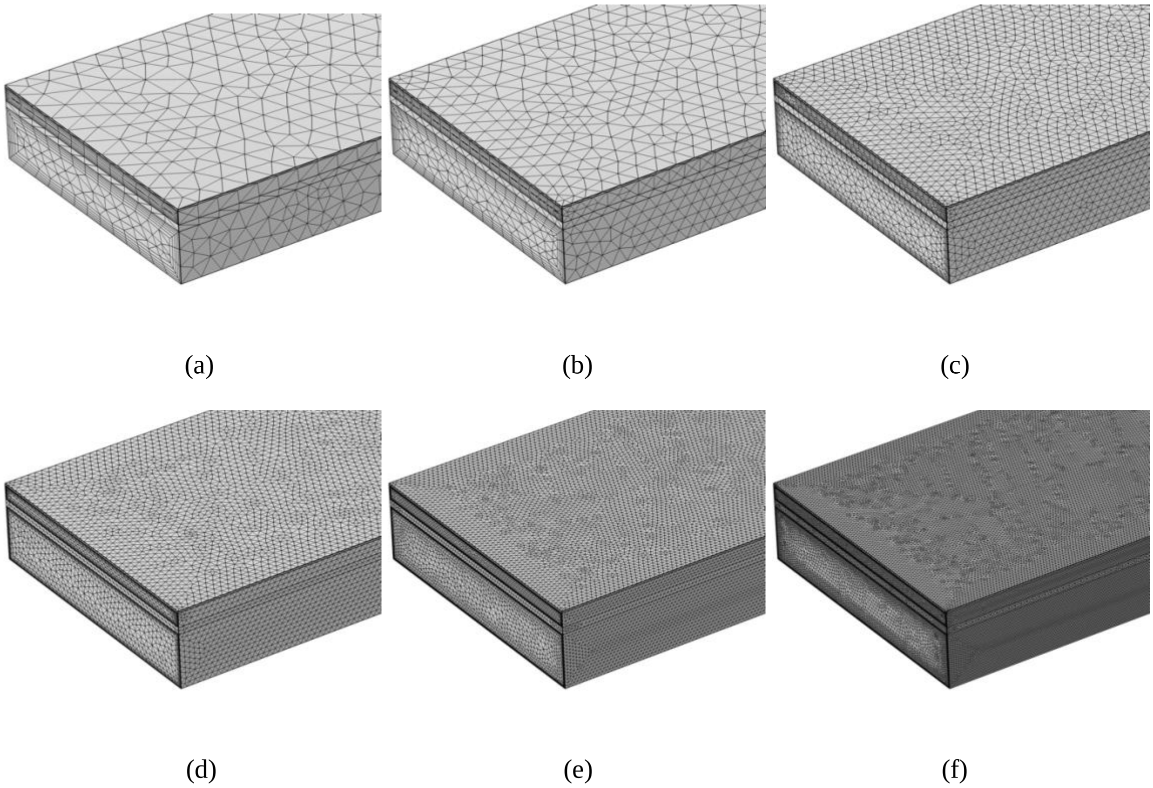

Fig 5. Generated mesh for DPSAH with mesh quality percentage (a) extremely coarse (56%) (b) Coarser (64%) (c) Coarse (67%) (d) Normal (71%) (e) Fine (75%) (f) Finer (81%)

Table 4. Validation between Ismail A.F et al.[32] and the CFD model

$\dot{m}$ (kg/s)	Irradiance (W/m^2)	Thermal Efficiency Range Ismail A.F et al. [32]	Thermal Efficiency Range CFD of This Work
0.015-0.06	500	51-67%	46-65%
0.015-0.06	600	50.5-66%	47-68.8%
0.015-0.06	700	50-65%	47.5-70%
0.015-0.06	800	50.1-66%	48.5-72%

Table 5. Thermophysical properties of Paraffin Wax PCM (RT47) [35]

Physical Properties	RT47
Melting temperature	41 – 48℃
Density solid	880 kg/m^3
Density fluid	770 kg/m^3
Specific heat	2000 J/kg.K
Thermal conductivity	0.2 W/m.K

3. Governing equations

3.1 Thermal Efficiency

The system's thermal energy efficiency can be determined by Eq. 12 [36]:

$$\eta_{\text{thermal}} = \frac{Qu}{(I\times A_c)} \tag{12}$$

Qu, the useful heat gain, can be calculated by Eq. 13 [36]:

$$Qu = \dot{m}C_p(T_o - T_i) \tag{13}$$

3.2 Electrical Efficiency

The system's electrical energy efficiency can be calculated by Eq. 14 [37]–[41]:

$$\eta_{\text{panel}} = \frac{P_{max}}{IA_c} \tag{14}$$

The extracted power can be estimated by Eqs. 15 - 16 [37]–[41]

$$P_{max} = I_m V_m = FFI_{sc}V_{oc} \tag{15}$$

$$= \eta_{\text{cell}}\, A_{\text{cells}}\, G\alpha_{pv}$$

$$\eta_{\text{cell}} = \eta_{\text{ref}}\left(1 - \beta_{\text{ref}}\left(T_{mpv} - T_{\text{ref}}\right)\right) \tag{16}$$

3.3 Combined Efficiency

The combined thermal and electrical efficiency can be computed using the following Eq. 17 [40]:

$$\eta_{co} = \eta_{th} + \frac{\eta_{ele}}{C_f} \tag{17}$$

Where C_f is the thermal power plant's conversion factor, which varies from 0.29 to 0.4 [42]. However, for the simulation purpose, the value was assumed to be approximately 0.36.

3.4 Reynolds Number (Re)

The Re number can be used to determine the flow regime in PVT-DPSAH. The Re number helps predict whether the fluid flow in the system will be laminar or turbulent, which affects the system's heat transfer efficiency and overall performance. Turbulent flow enhances heat transfer, promoting mixing and reducing thermal boundary layers, while the laminar flow is more predictable and easier to analyze mathematically. A high Re number indicates that the flow will be turbulent, with chaotic fluctuations in velocity and pressure, while a low Re number indicates that the flow will be laminar, with smooth, ordered layers of fluid. Reynold's number (Re) can be calculated as in Eq. 18 [42]:

$$Re = \frac{\dot{m}Dh}{Wd\mu} \tag{18}$$

Dh is the hydraulic diameter as in Eq. 19 [42], where d, and W are the equivalence height and width of the PVT-DPSAH.

$$Dh = \frac{4\,Wd}{2\,(W+d)} \tag{19}$$

4. Results and Discussion

The thermal efficiency, electrical efficiency, combined efficiency, velocity distribution, and the PCM charging temperature distribution in the bottom channel were evaluated through numerical investigations. Two methods were employed to confirm the accuracy of the results: a mesh independence study (table 3) and validation against prior research (Table 4). The model exhibits improved performance efficiencies, particularly with a higher mass flow rate.

4.1 Thermal Efficiency and Output Temperature

The outlet duct temperature and the suggested model's overall thermal efficiency are depicted in Fig 6. For the analysis, the reference temperature for the simulation was kept constant at 30ºC. The thermal efficiency was calculated using Eq. 12. Heat flux was set to 500, 600, 700, and 800 W/m^2 for different sets of tests. Simulations were performed with ṁ ranging from 0.015 kg/s to 0.065 kg/s. The data depicted in Fig 6 illustrates that when ṁ is increased, there is a noticeable improvement in thermal efficiency while the outlet temperature decreases. Notably, at solar irradiance levels of 500 W/m^2 to 800 W/m^2, the most effective ṁ is 0.037 kg/s. This results in an average thermal efficiency range of 60.7% to 63.4% and fluid output temperatures ranging from 42.96 ºC to 49.54 ºC at the optimum ṁ of 0.037 kg/s. According to Fudholi et al., a mass flow rate of approximately 0.03-0.09 kg/s is recommended for SAH systems [36].

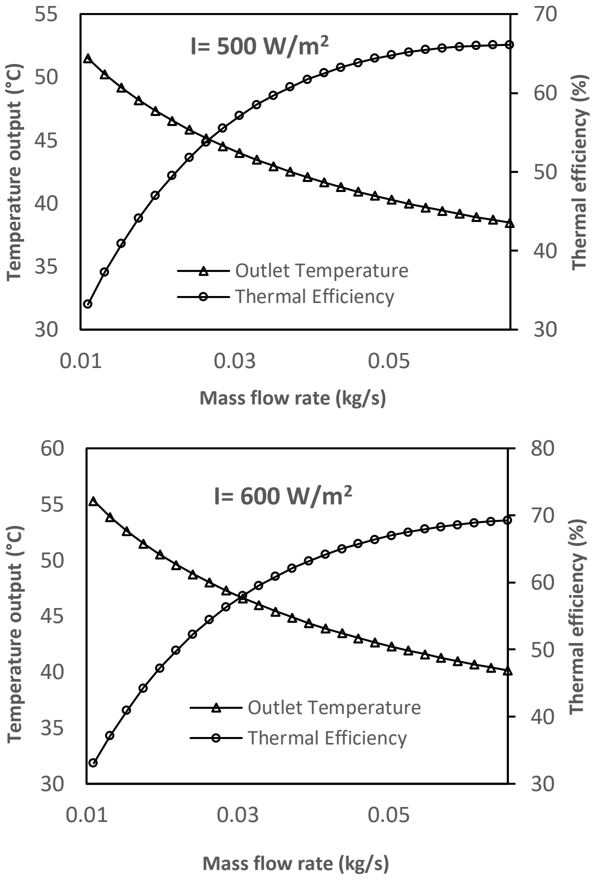

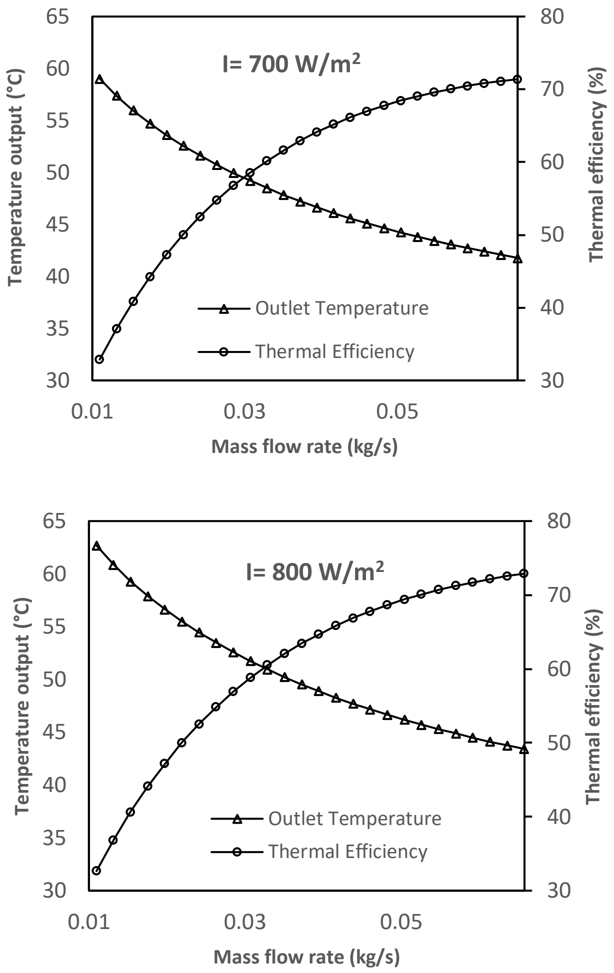

Fig. 6. Thermal efficiencies and output temperatures at various solar irradiance.

When testing the proposed collector under the heat flux 800 W/m^2, the thermal efficiency gradually increases from 32% to 72.88% as the $\dot{m}$ increases from 0.011 kg/s to 0.065 kg/s. With the flow rate of 0.065kg/s, the maximum thermal efficiency was 72.88%. The same pattern can be noticed for solar irradiances 500, 600 and 700 W/m^2, by increasing the flow rate the thermal efficiency increases while output temperature decrease. The outlet temperature decreases from 63 °C to 43 °C as the $\dot{m}$ increases from 0.011 kg/s to 0.065 kg/s for all the solar irradiances. As can be seen in Fig. 6, an increase in $\dot{m}$ has a more noticeable impact on thermal efficiency. However, the output temperature decreases as the flow rate increases. The current study results are well in range with the previous studies conducted by Ismail A.F et al. [32] and Assadeg et al. [33].

4.2 PV Surface Temperature

Figure 7 shows the PV surface temperature distribution for the optimum mass flow rate of 0.037 kg/s. Figure 8 shows that the PVT air collector temperature drops simultaneously as the $\dot{m}$ increases, leading to a lowered PV surface temperature. The highest temperatures are recorded at higher solar irradiances. Hence, solar irradiance is another element that affects the surface temperature of PV.

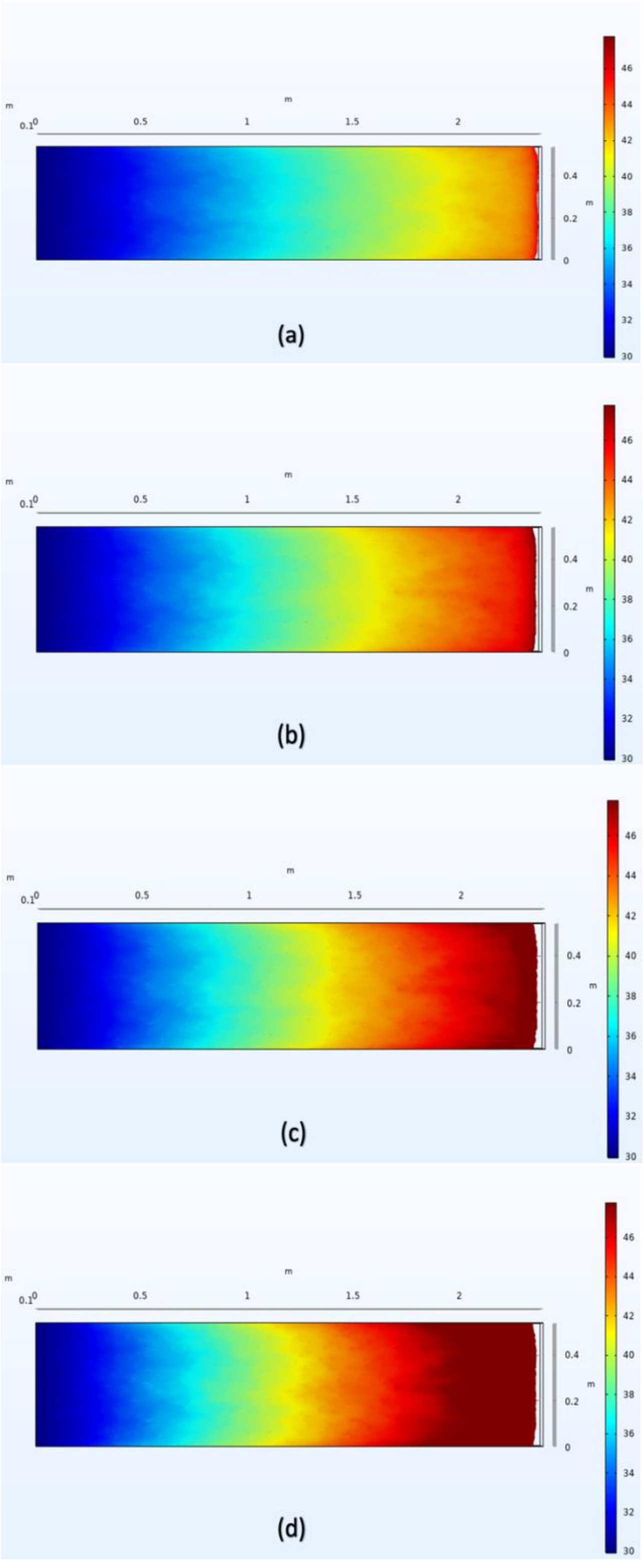

Fig 7. PV Surface Temperature at 0.037 kg/s (a) I = 500W/m^2 (b) I = 600W/m^2 (c) I = 700W/m^2 (d) I = 800W/m^2

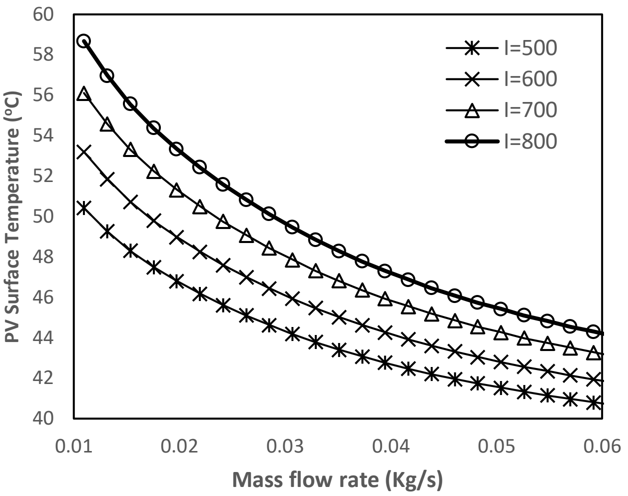

Fig 8. PV Surface Temperature changes with $\dot{m}$ for various solar irradiances.

However, the PVT-DPSAH is simulated under conditions of higher solar irradiation to achieve peak thermal and electrical efficiency. Othman et al. conducted theoretical and experimental analysis which demonstrates how the the intensity of the radiation affects the temperature increase for different flow rates. They found that for a specific $\dot{m}$, the temperature increase is proportional to the strength of the radiation [43].

4.3 Electrical and Combined Efficiency

The electrical efficiency was calculated using Eq. 14. Figure 9 presents the electrical efficiency of the PVT-DPSAH for different solar irradiances. Since the panel's efficiency is directly related to the mean temperature of the panel, the lowest panel temperature corresponds to the best electrical efficiency, which was achieved at 500 W/m^2. However, to operate the PVT-DPSAH for real-world use, higher solar irradiances are required for optimum performance. The efficiency gap is between 500 and 800 W/m^2, accounting for a 0.15% difference at a $\dot{m}$ of 0.065 kg/s. Figure 9 shows when the flow rate is increased, the heat transfer coefficient between the walls of the channel and the fluid increases, resulting in a decrease in the average temperature of the panel surface. Consequently, the collector's electrical efficiency will improve. In contrast to the rise in $\dot{m}$, the improvement in electrical efficiency is rather small. However, Figure 10 demonstrates that electrical efficiency does contribute to the system's overall efficiency.

The combined efficiency of the system was calculated using Eq. 17. Figure 10 shows how the mass flow rate affects the collector's combined efficiencies (thermal and electrical). The heat transfer coefficient improves with increasing air flow rate. The temperature of the PV panel drops as the flow rate rises, thus, improving the collector's efficiency. Figure 10 displays the maximum combined efficiency of PVT-DPSAH at 84.12% at 800 W/m^2 with a $\dot{m}$ of 0.065 kg/s. Othman et al. study shows the combined efficiency of PVT-DPSAH ranges from 39 to 70% when subjected to a $\dot{m}$ of 0.015-0.16 kg/s and a radiation intensity of 500 W/m^2 [43]. The current study combined efficiency ranges from 43% to 77% with solar irradiance of 500 W/m^2 under various flow rates. The results demonstrate the system's ability to efficiently convert solar energy into electricity while simultaneously generating the thermal energy for diverse applications. This study showcased an improved performance of PVT-DPSAH under different climatic parameters.

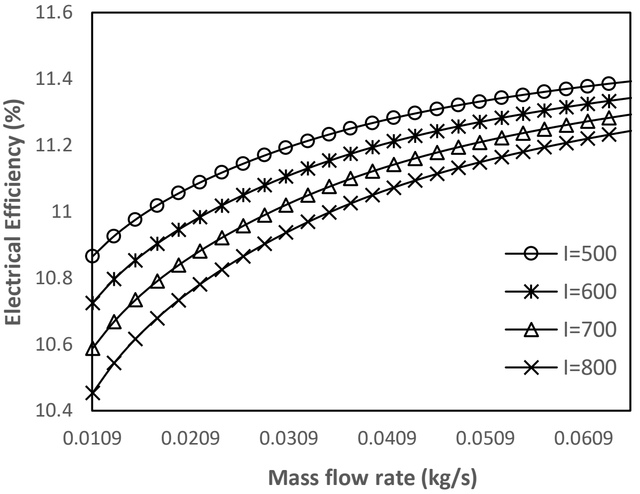

Fig 9. Electrical efficiency changes with the mass flow rate

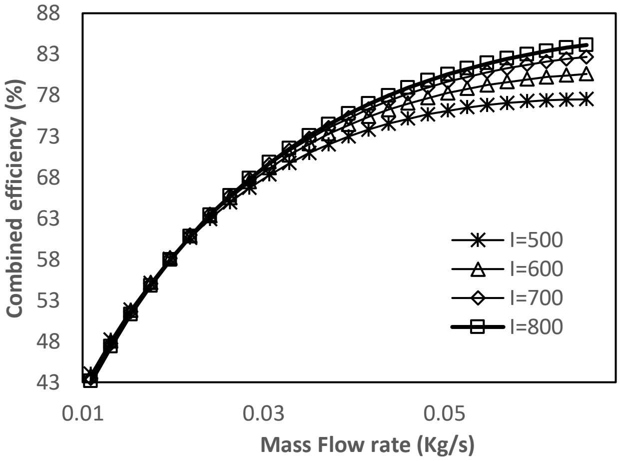

Fig 10. Combined (thermal and electrical) efficiency against various mass flow rates.

4.4 Velocity Distribution

Cylindrical PCM capsules were placed in a staggered configuration in the second channel. Heat is supplied to each section of the collecting absorber, and since the mass flow rate is uniform throughout the collectors, the fluid density decreases, and the flow velocity increases in the direction of the flow. The $\dot{m}$ depends on the inlet velocity, duct area, and air density. The inlet velocity for this simulation varied from (0.8 - 2.8 m/s) for various solar irradiances (500, 600, 700, and 800 W/m^2). Figure 11 displays the velocity patterns in the streamwise direction within the second channel. The inlet section of the second channel exhibits uniform flow velocity, while the velocity field appears almost indistinguishable across all areas surrounding the cylinders. The turbulent flow pattern can be seen around the cylinders. The Figure shows that the velocity near the edges of the cylinders slows down, and the velocity increases near the gap between the cylinders. Cylindrical capsules were chosen for this study because of their streamlined shape and symmetry, often used in aerodynamics to reduce drag and improve the flow of air or other fluids around them [44].

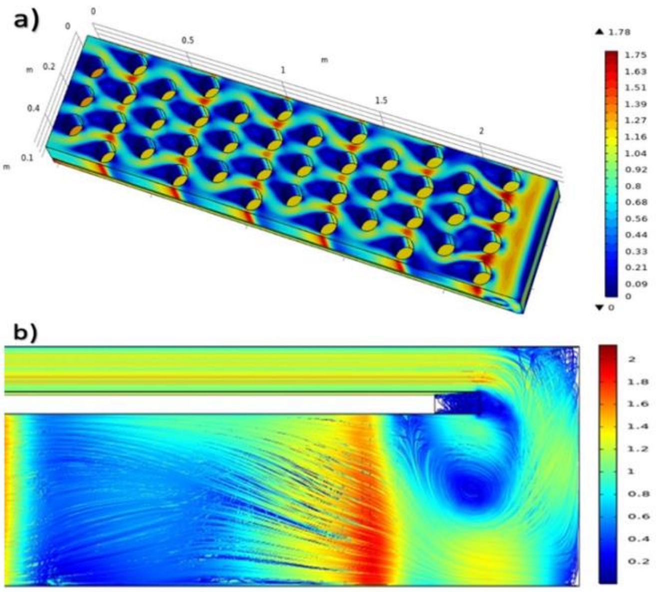

Fig 11. (a) (Top) Velocity distribution in the second channel, (b) (Bottom) Velocity streamline at the inlet of the second channel

4.5 Temperature Distribution in PCM Capsules

Based on the results of the optimum thermal efficiency and temperature distribution in the heater, paraffin wax RT47 was selected for the study. The thermophysical properties of paraffin wax RT47 were assumed to be constant and were defined in the COMSOL heat transfer node. Mass flow rate affects the charging of PCM in the second channel, with slower flow rates leading to greater charging. In order to increase PCM melting, a slower $\dot{m}$ is required. However, this reduces the heater's performance efficiency. Thus, for practical requirements, the heater should be operated with the optimal $\dot{m}$ ranging from 0.03 kg/s to 0.05 kg/s. Figure 12 (a), (b), and (c) shows the temperature distribution with the flow rates of 0.017, 0.037, and 0.065 kg/s, respectively, under the solar irradiance of 500 W/m^2. With increasing the $\dot{m}$ the ability to store heat is reduced, because the heat transfer co-efficient is increased which takes away the heat more quickly from the second channel. It can be seen from figure 12 (c) that the PCM is in solid state with the highest $\dot{m}$. The temperature distribution under solar irradiance of 600 W/m^2 is depicted in figure 12 (d), (e), and (f) for flow rates of 0.017, 0.037, and 0.065 kg/s, respectively. Figure 12 (f) shows promising results with the flow rate of 0.065 kg/s, it is observable that PCM capsules are in transition phase. The temperature distribution for varying flow rates of 0.017, 0.037, and 0.065 kg/s, correspondingly, under solar irradiance conditions of 700 W/m^2 and 800 W/m^2 are depicted in figure 13 (a), (b), (c) and (d), (e), (f), respectively. The PCM melting/charging results are very promising under higher solar irradiances, such as 700 and 800 W/m^2, even with the higher $\dot{m}$. For practical purposes, however, the system should be operated between 0.03 and 0.05 kg/s [33]. The optimal $\dot{m}$ for the current study was found to be 0.037 kg/s. From figures 12 and 13, with optimum $\dot{m}$ of 0.037 kg/s the PCM melting rate is high. A value of 1 indicates a fully charged PCM, while 0 represents the PCM in its solid state. This analysis gives us an insight into where to place the cylindrical PCM capsules in the second channel. Based on these results, the type of PCM that could be used practically in PVT-DPSAH can be determined.

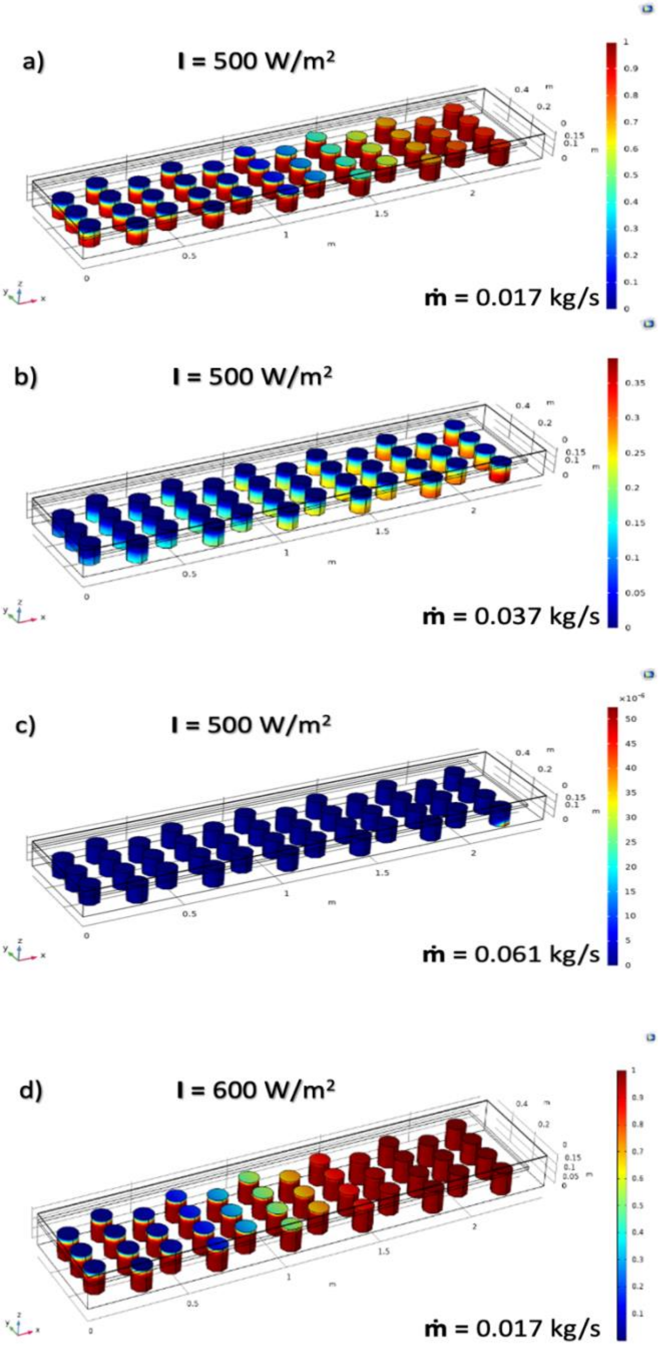

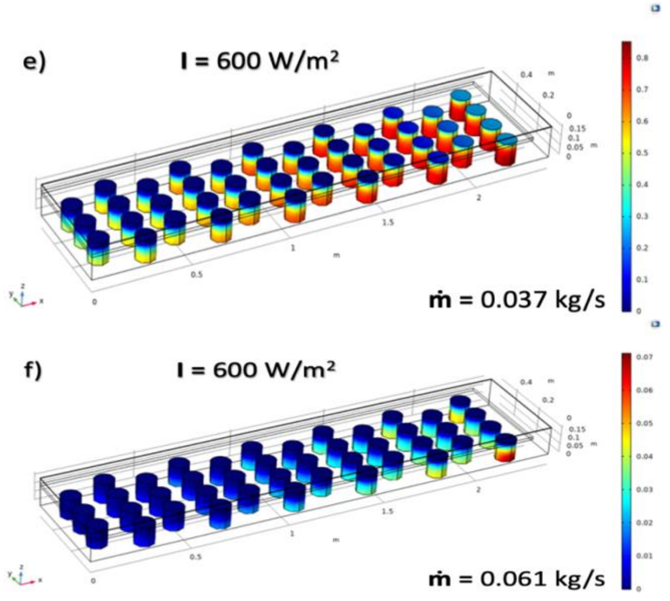

Fig 12. Temperature distribution in PCM capsules at 500 W/m^2 (a,b,c) and 600 W/m^2 (d,e,f)

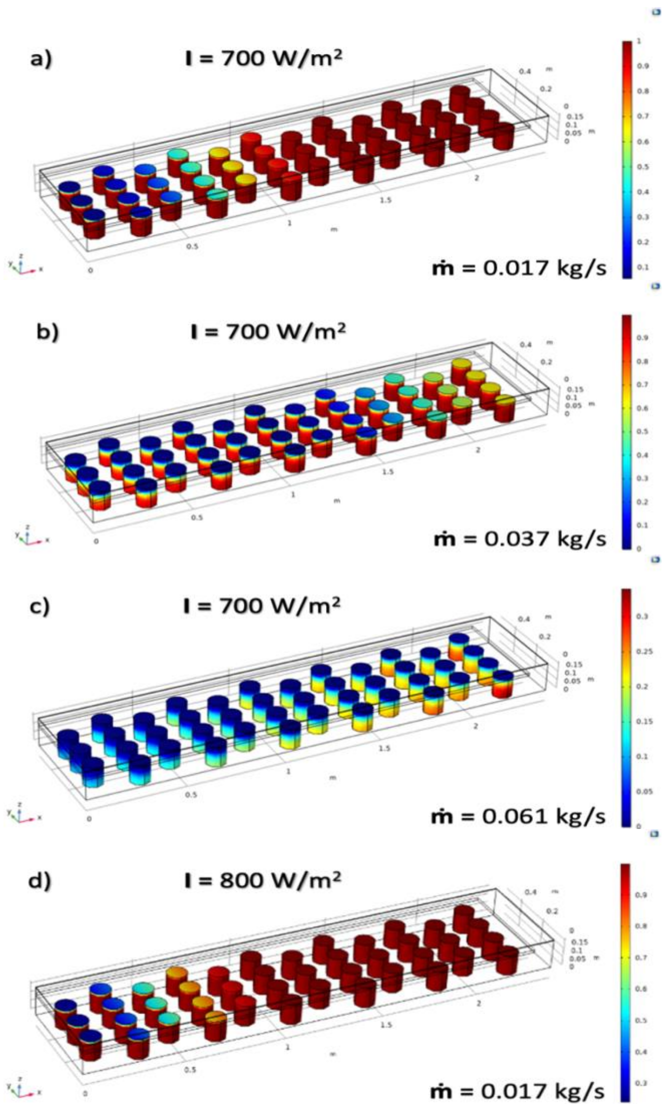

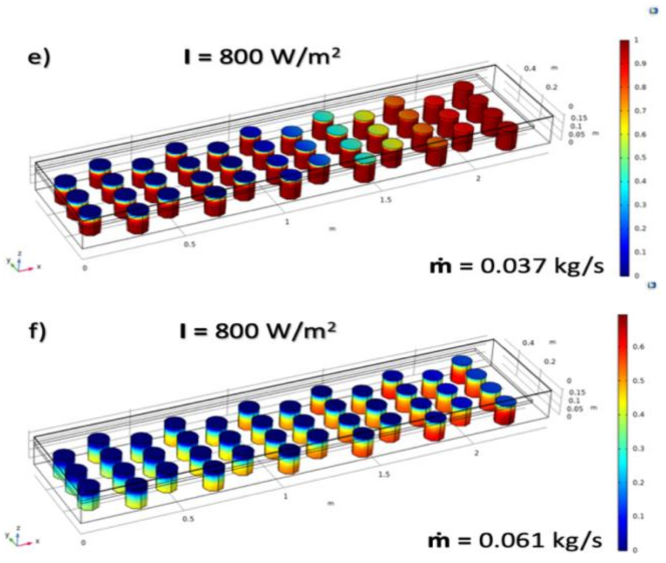

Fig 13. Temperature distribution in PCM capsules at 700 W/m^2 (a,b,c) and 800 W/m^2 (d,e,f).

5. Conclusion

This study presents a CFD investigation of a novel PVT-DPSAH through a steady-state FEM analysis design. The primary characteristics of this design are the PVT-DPSAH's PV collector and the second channel, which is equipped with vertical cylinder PCM capsules. The performance of the PVT-DPSAH collector was evaluated as the mass flow rate varied from 0.011 to 0.065 kg/s with solar irradiances of 500, 600, 700, and 800 W/m^2. The temperature distribution of the second channel was analyzed to determine the appropriate type of PCM to be used in the PVT-DPSAH. The major conclusions from the study are;

- The highest thermal efficiency achieved was 72.88% at 800 W/m^2 solar irradiance, with a $\dot{m}$ of 0.065 kg/s.
- The output temperature drops, and the system's thermal efficiency improves with increasing mass flow rates. Output temperatures were found to be at their lowest at $\dot{m}$ = 0.031- 0.065 kg/s and their highest at $\dot{m}$ = 0.011-0.031 kg/s.
- The highest electrical efficiency achieved was 11.39% at 500W/m^2, while the maximum combined efficiency obtained was 84.12% at 800 W/m^2 with a $\dot{m}$ of 0.065kg/s.
- PCM melting was more efficient, with an optimal $\dot{m}$ of 0.037 kg/s, indicating that the design is suitable for real-world use.
- Based on the temperature distribution results, RT-47-based PCM is selected for the study, showing greater charging potential at solar irradiances of 700 and 800 W/m^2.

Acknowledgements

The authors sincerely thank The Ministry of Higher Education of Malaysia for the financial support under Fundamental Research Grant Scheme - FRGS/1/2019/TK07/ UKM/02/4.

Nomenclature			
q_0	Heat transfer rate	u	Velocity
h	Heat tranfer coefficient	P_{max}	Maximum power ouput
T_{ext}	External Temperature	I	Solar Irradiance
k	Thermal conductivity	I_m	Maximum current output
L	Characteristic length	V_m	Maximum voltage output
RaL	Rayleigh number	A_c	Collector area
ρ	Density of the Material	FF	Fill factor
θ	Weight factors	I_{sc}	Short circuit current
c_p	Specific heat capacity	V_{oc}	Open current voltage
$L_{1\rightarrow 2}$	Heat transfer between phases	η_{cell}	Solar cell efficiency
α_m	Thermal expansion coefficient	A_{cells}	Total area of solar cells
μ_T	Turbulent viscosity	G	Solar irradiance
μ	Dynamic viscosity	α_{pv}	Absorption coefficient of solar cell
∇	Velocity gradient	η_{th}	Thermal efficiency
P_k	Production of kinetic energy	η_{ele}	Electrical efficiency
ϵ	Dissipation rate of turbulent kinetic energy	η_{co}	Combined efficiency
T_o	Outlet temperature	$(\eta_{\text{ref}}$	Reference electrical efficiency
T_i	Inlet temperature	P	Cells packing factor
β_{ref}	Temperature coefficient		

References

[1] E. Gul, G. Baldinelli, P. Bartocci, T. Shamim, P. Domenighini, F. Cotana, J. Wang, F. Fantozzi, F. Bianchi, “Transition toward net zero emissions - Integration and optimization of renewable energy sources: Solar, hydro, and biomass with the local grid station in central Italy” *Renewable Energy*, Volume 207, Pages 672-686, ISSN 0960-148, 2023.

[2] N. Faisal, A. S. A. amid, M. Arif, T. A. Khan, A. Naveed, M. Sadiq, S. Imad Ud din, and A. Ibrahim. 2022. “Solar–Biogas Microgrid: A Strategy for the Sustainable Development of Rural Communities in Pakistan,” *Sustainability* 14, no. 18: 11124, 2022.

[3] S. Kalogirou, “The potential of solar industrial process heat applications,” *Appl. Energy*, vol. 76, no. 4, pp. 337–361, 2003.

[4] V. V Tyagi, S. C. Kaushik, and S. K. Tyagi, “Advancement in solar photovoltaic/thermal (PV/T) hybrid collector technology,” *Renew. Sustain. Energy Rev.*, vol. 16, no. 3, pp. 1383–1398, 2012.

[5] V. Siva Reddy, S. C. Kaushik, K. R. Ranjan, and S. K. Tyagi, “State-of-the-art of solar thermal power plants—A review,” *Renew. Sustain. Energy Rev.*, vol. 27, pp. 258–273, 2013.

[6] M. A. A. Rahmat, A. S. A. Hamid, Y. Lu, M. Amir A. Ishak, S. Z. Suheel, A. Fazlizan, and A. Ibrahim, “An Analysis of Renewable Energy Technology Integration Investments in Malaysia Using HOMER Pro,” *Sustain.*, vol. 14, no. 20, 2022.

[7] K. O. Adu-Kankam, and L. Camarinha-matos, “Delegating Autonomy on Digital Twins in Energy Ecosystems,” *Int. J. Smart grid IJSMARTGRID*, vol. 6, no. 4, 2022.

[8] M. Kingsley-amaehule, R. Uhunmwangho, N. Nwazor, and E. Kenneth, “Smart Intelligent Monitoring and Maintenance Management of Photo-voltaic Systems,” *Int. J. Smart grid IJSMARTGRID*, vol. 6, no. 4, 2022.

[9] S. A. Nagalkar, A. B. Kanase-Patil, and N. A. Phadtare, “Heat transfer enhancement in solar air heater having multi-arc shape artificial roughness with gap,” in *2015 International Conference on Technologies for Sustainable Development (ICTSD)*, 2015, pp. 1–6.

[10] L. B. Y. Aldabbagh, F. Egelioglu, and M. Ilkan, “Single and double pass solar air heaters with wire mesh as packing bed,” *Energy*, vol. 35, no. 9, pp. 3783–3787, 2010.

[11] A. A. El-Sebaii, S. Aboul-Enein, M. R. I. Ramadan, S. M. Shalaby, and B. M. Moharram, “Thermal performance investigation of double pass-finned plate solar air heater,” *Appl. Energy*, vol. 88, no. 5, pp. 1727 1739, 2011.

[12] M. K. Hussain, A. M. Rasham, and B. M. Alshadeedi, “Finite Element Modeling Of Finned Double-Pass Solar Air Heaters,” in *2021 4th International Conference on Energy Conservation and Efficiency (ICECE)*, 2021, pp. 1–6.

[13] A. Fudholi, M. H. Ruslan, M. Y. Othman, M. Yahya, Supranto, A. Zaharim, and K. Sopian, “Experimental study of the double-pass solar air collector with staggered fins,” Int. Conf. *Syst. Sci. Simul. Eng. - Proc.*, no. February 2015, pp. 410–414, 2010.

[14] A. Fudholi, K. Sopian, M. Y. Othman, M. H. Ruslan, and B. Bakhtyar, “Energy analysis and improvement potential of finned double-pass solar collector,”

Energy Convers. Manag., vol. 75, pp. 234–240, 2013.

[15] A. M. Bassam, K Sopian, A Ibrahim, M Faizal Fauzan, A. B. Al-Aasam, and G. Y. Abusaibaa, “Experimental analysis for the photovoltaic thermal collector (PVT) with nano PCM and micro-fins tube nanofluid,” *Case Stud. Therm. Eng.*, vol. 41, no. August 2022, p. 102579, 2023.

[16] F. S. Javadi, H. S. C. Metselaar, and P. Ganesan, “Performance improvement of solar thermal systems integrated with phase change materials (PCM), a review,” *Sol. Energy*, vol. 206, pp. 330–352, 2020.

[17] F. Javed, “Impact of Temperature & Illumination for Improvement in Photovoltaic System Efficiency,” *Int. J. Smart grid IJSMARTGRID*, vol. 6, no. v6i1, 2022.

[18] S. Riffat, B. Mempouo, and W. Fang, “Phase change material developments: a review,” *Int. J. Ambient Energy*, vol. 36, 2013.

[19] T. Klemm, A. Hassabou, A. Abdallah, O. Andersen, “Thermal energy storage with phase change materials to increase the efficiency of solar photovoltaic modules,” *Energy Procedia*, vol. 135, pp. 193–202, 2017.

[20] M. Naderi, B. M. Ziapour, M. Y. Gendeshmin, “Improvement of photocells by the integration of phase change materials and thermoelectric generators (PV-PCM-TEG) and study on the ability to generate electricity around the clock,” *J. Energy Storage*, vol. 36, no. October 2020, p. 102384, 2021.

[21] A. K. Goel, S. N. Singh, B. N. Prasad, “Experimental investigation of thermo-hydraulic efficiency and performance characteristics of an impinging jet-finned type solar air heater,” *Sustain. Energy Technol. Assessments*, vol. 52, no. PB, p. 102165, 2022.

[22] S. Singh, “Experimental and numerical investigations of a single and double pass porous serpentine wavy wiremesh packed bed solar air heater,” *Renew. Energy*, vol. 145, pp. 1361–1387, 2020.

[23] M. Al-Damook, Z. A. H. Obaid, M. Al-Qubeissi, D. Dixon-Hardy, J. Cottom, P. J. Heggs, “CFD modeling and performance evaluation of multipass solar air heaters,” *Numer. Heat Transf. Part A Appl.*, vol. 76, no. 6, pp. 438–464, 2019.

[24] E. Touti, M. Masmali, M. Fterich, H. Chouikhi, “Experimental and numerical study of the PVT design impact on the electrical and thermal performances,” *Case Stud. Therm. Eng.*, vol. 43, no. January, p. 102732, 2023.

[25] A. S. Yadav, T. Alam, G. Gupta, R. Saxena, N. K. Gupta, K. V. Allamraju, R. Kumar, N. Sharma, A. Sharma, U. Pandey, and Y. Agrawal, “A Numerical Investigation of an Artificially Roughened Solar Air Heater,” *Energies*, vol. 15, no. 21, 2022.

[26] A. S. Yadav and J. L. Bhagoria, “Modeling and Simulation of Turbulent Flows through a Solar Air Heater Having Square-Sectioned Transverse Rib Roughness on the Absorber Plate,” *Sci. World J.*, vol. 2013, p. 827131, 2013.

[27] A. S. Yadav, J. L. Bhagoria, “A CFD (computational fluid dynamics) based heat transfer and fluid flow analysis of a solar air heater provided with circular transverse wire rib roughness on the absorber plate,” *Energy*, vol. 55, pp. 1127–1142, 2013.

[28] S. A. Nagalkar, A. B. Kanase-Patil, and N. A. Phadtare, “Heat transfer enhancement in solar air heater having multi-arc shape artificial roughness with gap,” in *2015 International Conference on Technologies for Sustainable Development (ICTSD)*, 2015, pp. 1–6.

[29] A. Ibrahim, M. Y. Othman, M. H. Ruslan, S. Mat, K. Sopian, “Recent advances in flat plate photovoltaic/thermal (PV/T) solar collectors,” *Renew. Sustain. Energy Rev.*, vol. 15, no. 1, pp. 352–365, 2011.

[30] A. D. Tuncer, A. Khanlari, A. Sözen, E. Y. Gürbüz, C. Şirin, A. Gungor, “Energy-exergy and enviro-economic survey of solar air heaters with various air channel modifications,” *Renew. Energy*, vol. 160, pp. 67–85, 2020.

[31] J. A. Ghani, F. F. Mohd Nasir, H. A. Rahman, W. F. H. W. Zamri, M. S. Kasim, S. S. Muhamad, “Computational fluid dynamic analysis on tribological performance under hydrodynamic lubrication of dimple textured surface produced using turning process,” *Wear*, vol. 477, no. April, p. 203898, 2021.

[32] A. F. Ismail, A. S. A. Hamid, A. Ibrahim, H. Jarimi, K. Sopian, “Performance Analysis of a Double Pass Solar Air Thermal Collector with Porous Media Using Lava Rock,” *Energies*, vol. 15, no. 3, 2022.

[33] J. Assadeg, Ali H. A. Al-Waeli, A. Fudholi, K. Sopian, “Energetic and exergetic analysis of a new double pass solar air collector with fins and phase change material,” *Sol. Energy*, vol. 226, pp. 260–271, 2021.

[34] M. García-Fuente, D. González-Peña, C. Alonso-Tristán, “A Numerical Simulation of an Experimental Melting Process of a Phase-Change Material without Convective Flows,” *Appl. Sci.*, vol. 12, no. 7, 2022.

[35] H. Niazmand, H. Talebian, M. Mahdavikhah, “Bed

geometrical specifications effects on the performance of silica/water adsorption chillers," *Int. J. Refrig.,* vol. 35, no. 8, pp. 2261–2274, 2012.

[36] A. Fudholi, K. Sopian, M. H. Ruslan, M. Y. Othman, "Performance and cost benefits analysis of double-pass solar collector with and without fins," *Energy Convers. Manag.*, vol. 76, pp. 8–19, 2013.

[37] A. H. Jaaz, K. Sopian, T. S. Gaaz, "Study of the electrical and thermal performances of photovoltaic thermal collector-compound parabolic concentrated," *Results in Physics*, Volume 9, Pages 500-510, ISSN 2211-3797, 2018.

[38] M. M. Matheswaran, T. V. Arjunan, D. Somasundaram, "Analytical investigation of solar air heater with jet impingement using energy and exergy analysis," *Sol. Energy*, vol. 161, no. October 2017, pp. 25–37, 2018.

[39] A. R. A. Elbar, H. Hassan, "Energy, exergy and environmental assessment of solar still with solar panel enhanced by porous material and saline water preheating," *J. Clean. Prod.*, vol. 277, p. 124175, 2020.

[40] W. E. Ewe, A. Fudholi, K. Sopian, R. Moshery, N. Asim, W. Nuriana, A. Ibrahim, "Thermo-electro-hydraulic analysis of jet impingement bifacial photovoltaic thermal (JIBPVT) solar air collector," *Energy*, vol. 254, p. 124366, 2022.

[41] N. S. Nazri, A. Fudholi, B. Bakhtyar, C. H. Yen, A.Ibrahim, M. H. Ruslan, S. Mat, and K. Sopian, "Energy economic analysis of photovoltaic-thermal-thermoelectric (PVT-TE) air collectors," *Renew. Sustain. Energy Rev*., vol. 92, no. April, pp. 187–197, 2018.

[42] A. Fudholi, M. Zohri, N. S. B. Rukman, N. S. Nazri, M. Mustapha, C. H. Yen, M. Mohammad, K. Sopian, "Exergy and sustainability index of photovoltaic thermal (PVT) air collector: A theoretical and experimental study," *Renew. Sustain. Energy Rev*., vol. 100, no. July 2018, pp. 44–51, 2019.

[43] M. Yusof, M. Y. Othman, B. Yatim, K. Sopian, M. N. A. Bakar, Performance Analysis Of a Double-Pass Photovoltaic/Thermal (PV/T) Solar Collector with CPC and Fins, *Renewable Energy*, Volume 30, Issue 13, Pages 2005-2017, ISSN 0960-1481,2005.

[44] C. Demartino, F. Ricciardelli, Aerodynamics of nominally circular cylinders: A review of experimental results for Civil Engineering applications, *Engineering Structures*, Volume 137, Pages 76-114, ISSN 0141-0296, 2017.